Chinese Chemical Letters 35 (2024) 109452

Contents lists available at ScienceDirect

Chinese Chemical Letters

journal homepage: www.elsevier.com/locate/cclet

D-A-D-structured boron-dipyrromethene with aggregation-induced enhanced phototherapeutic efficiency for near-infrared fluorescent and photoacoustic imaging-guided synergistic photodynamic and photothermal cancer therapy

Xuejian Xing[a,b,1], Pan Zhu[a,1], E Pang[a], Shaojing Zhao[a], Yu Tang[a], Zheyu Hu[c,d], Quchang Ouyang[c,d,*], Minhuan Lan[a,*]

[a] Key Laboratory of Hunan Province for Water Environment and Agriculture Product Safety, College of Chemistry and Chemical Engineering, Central South University, Changsha 410083, China
[b] School of Chemistry and Chemical Engineering, Neijiang Normal University, Neijiang 641100, China
[c] Medical Department of Breast Cancer, Hunan Cancer Hospital, Changsha 410083, China
[d] Medical Department of Breast Cancer, The Affiliated Cancer Hospital of Xiangya School of Medicine, Central South University, Changsha 410083, China

ARTICLE INFO

Article history:
Received 26 September 2023
Revised 21 December 2023
Accepted 22 December 2023
Available online 26 December 2023

Keywords:
Boron-dipyrromethene
Aggregation
Intersystem crossing
Twisted intramolecular charge transfer
Photodynamic therapy
Photothermal therapy

ABSTRACT

Clinical phototheranostic agents suffer from low absorption in near-infrared (NIR) region, decreasing singlet oxygen quantum yield ($^1O_2$ QY) caused by aggregation in water, and low photothermal conversion efficiency (PCE), all of which are factors weakening their phototheranostic efficacy. Herein, we designed and synthesized a donor-acceptor-donor (D-A-D) structured boron-dipyrromethene derivative (**B-2TPA**) which exhibited NIR absorption and fluorescence. After being encapsulated in amphiphilic distearoyl phosphoethanolamine polyethyleneglycol 2000 (DSPE-PEG-2000), the water-soluble **B-2TPA** nanoparticles (NPs) had increasing $^1O_2$ QY (6.7%) due to the intermolecular aggregation-induced decrease in the energy gap between singlet and triplet excited states. Moreover, the quenched fluorescence and stable twisted intramolecular charge transfer in aggregates further increased the PCE of **B-2TPA** NPs to 60.1%. *In vitro* and *in vivo* studies confirmed that **B-2TPA** NPs could be used in NIR fluorescence and photoacoustic imaging-guided synergistic photodynamic and photothermal therapy in tumor treatment.

Phototheranostics, as a novel cancer treatment technology, has the advantages of precise spatiotemporal control, efficient diagnosis and treatment, non-invasive, negligible drug resistance, and weak side effects. Upon laser irradiation, phototheranostic agents generate fluorescence for imaging guided diagnosis of tumors [1,2]. These agents also produce cytotoxic reactive oxygen species (ROS) through photodynamic therapy (PDT) or convert photo-energy into heat by photothermal therapy (PTT) to kill tumors [3,4]. Red-shift in absorption and fluorescence spectra, enhancement of ROS generation capability, and increasing photothermal conversion efficiency (PCE) of phototheranostic agents can improve imaging quality and phototheranostic efficacy. Moreover, the combination of PDT and PTT can further improve the therapeutic efficacy because increasing temperature in PTT can accelerate blood flow rate and alleviate oxygen depletion in tumor tissue to improve PDT efficacy [5,6]. Meanwhile, the ROS generation in PDT is advantageous to PTT as it can destroy the structure and biological function of heat shock proteins [7].

Porphyrins have been clinically approved for use in PDT due to their high singlet oxygen quantum yield ($^1O_2$ QY) [8,9]. However, their poor water-solubility and large planar π-conjugate structure triggers the formation of aggregates in water through tight intermolecular π-π stacking [10,11], which results in undesirable aggregation-induced quenching (ACQ) that inhibits ROS generation and fluorescence emission [12]. Recent reports suggested that indocyanine green (ICG) can be used as phototheranostic agent for fluorescent imaging-guided PDT and PTT [13,14]. However, its poor photostability, low PCE and $^1O_2$ QY lead to decreasing phototherapeutic efficacy [15,16]. Thus, the development of novel phototheranostic agents with strong near-infrared (NIR) absorption and fluo-

* Corresponding authors.
E-mail addresses: oyqc1969@126.com (Q. Ouyang), minhuanlan@csu.edu.cn (M. Lan).
[1] These authors contributed equally to this work.

https://doi.org/10.1016/j.cclet.2023.109452
1001-8417/

rescence, high $^1O_2$ QY and PCE, and excellent photostability is urgent.

Electron-donating and electron-withdrawing groups can be simultaneously introduced into one molecule to construct a donor-acceptor-donor (D-A-D) system, causing a narrow band gap of molecule, thus this is a simple and feasible method for preparing NIR phototheranostic agents [17–19]. For example, Zhao *et al.* used 4,4′-(2,2-diphenylethene-1,1-diyl)bis(*N*,*N*-diphenylaniline) and benzobisthiadiazole as the electron-donating and electron-withdrawing groups, respectively, for constructing an aggregation-induced emission (AIE) fluorogen DDTB (λ_{abs} = 650 nm, λ_{Em} = 973 nm), and then prepared it into water-soluble nanoparticles (NPs). The fluorescence and $^1O_2$ QYs of DDTB NPs are increased to 0.96% and 1.05%, respectively, which are higher than that of DDTB in molecularly dispersed state. However, the vibration relaxation of DDTB was restricted in aggregates, leading to a low PCE of 30.7% [20]. Aggregate-induced decrease in energy gap between the excited singlet (S_1) and triplet (T_1) state is a promising strategy that can solve decreasing $^1O_2$ QY caused by ACQ effect [21,22]. Guo *et al.* reported a Ru(II)-arene compound (λ_{abs} = 729 nm, λ_{Em} = 1050 nm) that has no photosensitive activity in molecularly dispersed state but can generate $^1O_2$ with a QY of 16.4% in aggregate state [23]. Theoretical calculation results suggested that the enhancement of intersystem crossing (ISC) in aggregate state is caused by decreasing energy gap from S_1 to T_1 (ΔE_{ST}). However, its PCE is only 24.2%, making it impossible to achieve ideal PTT efficacy.

The effective intramolecular motion facilitates vibration relaxation, enhancing the PCE of molecule [24]. Chen *et al.* maximized the intramolecular motion of Py-PS by introducing multiple stretchable and vibrational groups, achieving a high PCE of 86.8% [25]. Peng *et al.* synthesized tfm-BDP by introducing trifluoromethyl at the *meso* site of boron-dipyrromethene (BODIPY). Due to the rotation-free mechanism of trifluoromethyl in the aggregation, the PCE of tfm-BDP reaches to 88.3% [26]. In addition, it has been reported that the spatial configuration of excited fluorogen with D-A structure is changed due to intramolecular rotation, resulting in twisted intramolecular charge transfer (TICT) effect [27,28], in which the fluorescence QY of fluorogen decreased and the absorbed photo-energy is released through vibration relaxation. Therefore, TICT effect can significantly improve the photothermal conversion ability of photothermal agents [29]. Tang *et al.* proposed an "intramolecular motion in aggregate" strategy and designed four compounds (NIR6, NIRb6, NIRb10, and NIRb14) with NIR absorption by introducing molecular rotors and alkane chains into D-A molecules [30]. The long alkane chains served as steric hindrance groups that prevent tight intermolecular π-π stacking [31]. Among all compounds, NIRb14 has the highest PCE of 31.2% due to obvious fluorescence quenching and stable TICT in aggregates. Recently, we designed and synthesized a hemicyanine dye (M1, λ_{abs} = 714 nm, λ_{Em} = 1005 nm) with D-π-A structure [32]. The *tert*-butyl group on cyclohexene and two methyl groups on furan stabilize the rotation of M1 by effectively preventing tight intermolecular π-π stacking [33], in turn increasing the photothermal conversion ability of M1 NPs (PCE = 77.5%). Thus, the combination of "aggregation-induced decrease of ΔE_{ST}" and "intramolecular motion in aggregate" is an advanced strategy for constructing phototheranostic agents with excellent ROS generation capability and high PCE.

Based on the above considerations, herein, both aggregation-induced increase in singlet-triplet ISC and TICT effect were simultaneously used to develop phototheranostic agents with strong NIR absorption, aggregation-induced enhancement of $^1O_2$ QY and PCE. We selected *N*,*N*-diethylaniline and triphenylamine as electron-donating groups, and the core structure of BODIPY as electron-withdrawing group to design and synthesize a D-A-D structured BODIPY derivative (named **B-2TPA**) with NIR absorption and fluorescence peaks at 729 and 766 nm, respectively, and TICT effect (Fig. 1a). Under 735 nm laser irradiation, **B-2TPA** had low $^1O_2$ QY of 1.8% and PCE of 39.8%. After being assembled with DSPE-PEG-2000, these **B-2TPA** NPs exhibited excellent water dispersibility, red-shifted absorption and fluorescence spectra. Moreover, the intermolecular aggregation in **B-2TPA** NPs effectively decreased the ΔE_{ST} and significantly improved the ISC efficiency, resulting in an increase of $^1O_2$ QY to 6.7%. In addition, obvious fluorescence quenching and stable TICT in **B-2TPA** NPs also enhanced the PCE to 60.1%. Furthermore, **B-2TPA** NPs had excellent photostability, and strong NIR fluorescence and photoacoustic (PA) signals. Both *in vitro* and *in vivo* experiments demonstrated that **B-2TPA** NPs were suitable for synergistic PDT and PTT, as well as in dual-mode NIR fluorescence and PA imaging of tumor (Fig. 1b).

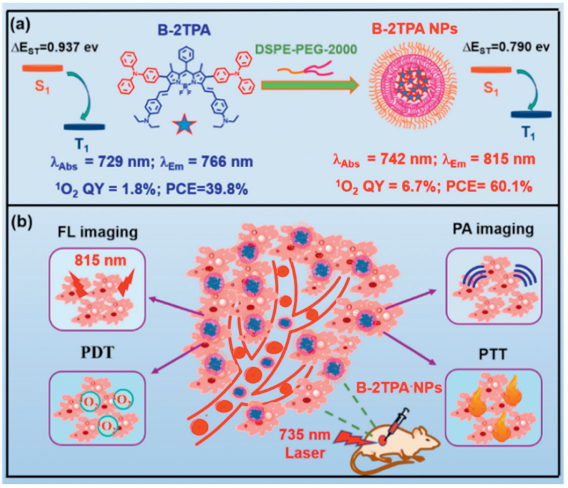

Fig. 1. (a) Preparation of **B-2TPA** NPs, and molecular structure and main optical properties of **B-2TPA** and **B-2TPA** NPs. (b) Application of **B-2TPA** NPs in NIR fluorescence and PA imaging-guided synergistic PDT and PTT of tumor.

Phototheranostic agents with an aggregation-induced increase in $^1O_2$ QY and good photothermal conversion ability are greatly advantageous to cancer therapy. Herein, **B-2TPA** for phototheranostic application has the following advantages: (1) The introduction of strong electron-donating groups (*N*,*N*-diethylaniline and triphenylamine) into the core structure of BODIPY to construct a D-A-D system allows the absorption and fluorescence wavelengths of **B-2TPA** to locate in the NIR region [34]. (2) As shown in optimized ground state (S_0) geometry figure of **B-2TPA** (Fig. 2a), the large dihedral angle between triphenylamine and BODIPY causes large non-planar π-conjugated structure of **B-2TPA**, which not only avoids the tight face-to-face π-π stacking in water [35], but also triggers the formation of **B-2TPA** NPs through simple intermolecular aggregation, resulting in decreasing energy gap between S_1 and T_n, thus allowing the enhancement of ISC efficiency, in turn increasing the $^1O_2$ QY of **B-2TPA** NPs; and (3) **B-2TPA** has high liposolubility and multiple rotational structures; thus, in the hydrophobic microenvironment formed by long-chain alkanes of DSPE-PEG-2000, the PCE of **B-2TPA** aggregates is enhanced due to obvious fluorescence quenching and stable TICT effect [24]. The synthetic route of **B-2TPA** is shown in Scheme S1 (Supporting information). All the obtained compounds were characterized by ^1H nuclear magnetic resonance (NMR), ^{13}C NMR (Figs. S1–S8 in Supporting information), and high-resolution mass spectrometry (HRMS).

The absorption and fluorescence spectra of **B-2TPA** were measured, and the results are shown in Fig. 2b. Due to the strong ICT effect and large π-conjugated structure, the absorption and fluorescence wavelengths of **B-2TPA** in 1,4-dioxane were 729 and 766 nm, respectively. Upon photoexcitation, the molecules with TICT

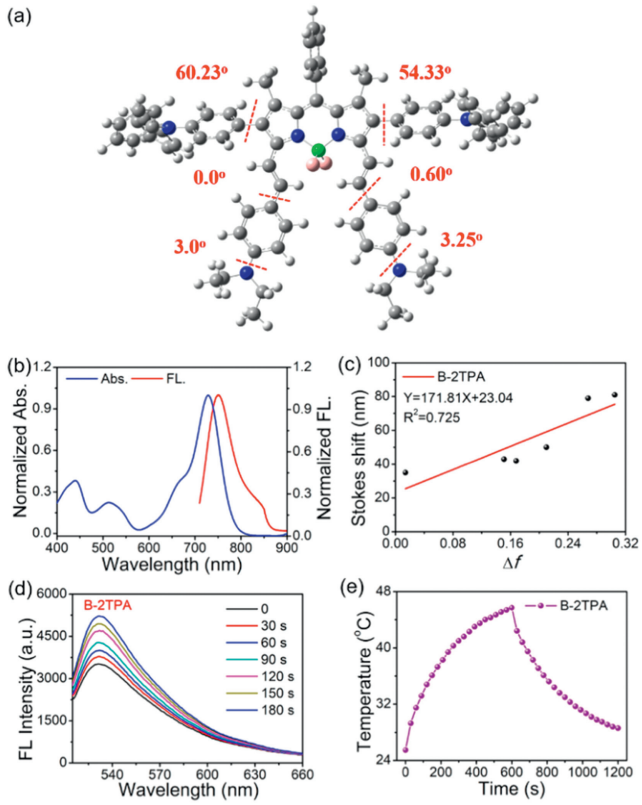

Fig. 2. (a) Optimized ground state (S_0) geometries of **B-2TPA**. (b) Normalized visible (vis)-NIR absorption and fluorescence spectra of **B-2TPA** in 1,4-dioxane. (c) Line-fitting of a plot between Stokes shift and Δf. (d) Irradiation time-dependent fluorescence change of SOSG in **B-2TPA** solution. (e) Irradiation time-dependent temperature variation of **B-2TPA** solution.

effect first are in a locally excited state, and then undergo structural twist to enter the TICT state, inducing the locally excited-state and TICT emission of molecule in moderately polar solvents can be observed [36]. Thus, the trailing of fluorescence spectrum of **B-2TPA** (800–900 nm) in dioxane is caused by its TICT effect.

To further demonstrate the TICT effect of **B-2TPA**, the influence of solvent on the optical properties of **B-2TPA** was studied. As shown in Fig. S9 (Supporting information), with the solvent polarity increased, the absorption and fluorescence wavelengths of **B-2TPA** were red-shifted from 717 and 759 nm (in diethyl ether) to 749 and 831 nm (in DMSO), respectively, while its fluorescence intensity decreased from 585.5 K (in diethyl ether) to 77.0 K (in DMSO), which is indicative of obvious solvatochromic effect of **B-2TPA** [37]. To quantitatively evaluate the effect of solvent polarity on fluorescence behavior, the Lippert-Mataga equation, which directly represents the relationship of Stokes shift of fluorogen in different solvents between solvent polarity parameters (Δf) was used [38], and the results are displayed in Fig. 2c and summarized in Table S1 (Supporting information). The Stokes shift gradually increased with increasing solvent polarity parameter, indicating the significant TICT effect of **B-2TPA**. Additionally, the molar extinction coefficient of **B-2TPA** was 1.15×10^5 L mol^{-1} cm^{-1}. Using zinc phthalocyanine (Zn-Pc) as a reference, the fluorescence QY of **B-2TPA** in 1,4-dioxane was measured to be 22.6% (Fig. S10 and Table S2 in Supporting information).

The $^1O_2$ generation capability of **B-2TPA** upon 735 nm laser irradiation was investigated using singlet oxygen sensor green (SOSG) as the $^1O_2$ trapper. As shown in Fig. 2d, the green fluorescence originated from SOSG in the mixture solution of **B-2TPA**-SOSG gradually increased with increasing irradiation time. The $^1O_2$ QY of **B-2TPA** was 1.8% using ICG as a reference (Fig. S11 in Supporting information) [39]. Moreover, **B-2TPA** exhibited excellent photostability. As revealed in Fig. S12 (Supporting information), after irradiation with 735 nm laser with a power of 1.0 W/cm^2 for 10 min, the absorption spectra of **B-2TPA** showed almost no change. Moreover, the temperature of **B-2TPA** solution rose from 25.8 °C to 45.7 °C (Fig. 2e), and its PCE in dioxane was calculated to be 39.8% ± 0.9% (Fig. S13 in Supporting information).

B-2TPA was encapsulated in the amphiphilic DSPE-PEG-2000 to prepare water-soluble **B-2TPA** NPs, and the encapsulation yield of that in NPs is 88.3%. The spherical morphology of **B-2TPA** NPs was observed by scanning electron microscope (SEM) (Fig. S14a in Supporting information). The size distribution of **B-2TPA** NPs is ranged from 32 nm to 397 nm (Fig. S14b in Supporting information). The average size of **B-2TPA** NPs measured by dynamic light scattering (DLS) was ~120 nm, and no obvious changes were observed within one week of observation in aqueous solution, which is indicative of their excellent long-term stability (Fig. S14c in Supporting information). The absorption and fluorescence peaks of **B-2TPA** NPs red-shifted to 742 and 815 nm, respectively (Fig. 3a). Moreover, the trailing of fluorescence spectrum of **B-2TPA** NPs (900–1000 nm) caused by TICT effect was also observed. Interestingly, these **B-2TPA** NPs can still generate $^1O_2$ under 735 nm laser irradiation. Compared to **B-2TPA** in the molecular state, the $^1O_2$ QY of **B-2TPA** NPs was enhanced by 3.7 times, reaching to 6.7% (Fig. 3b and Fig. S15 in Supporting information).

To understand the mechanism of aggregation-induced enhancement of $^1O_2$ QY, the electronic characteristics and properties in excited state of monomeric and dimeric **B-2TPA** were investigated by theoretical calculation. The frontier molecular orbitals were acquired *via* density functional theory (DFT) calculations at B3LYP-D3BJ/6-311G*, and the results were shown in Fig. 3c. As observed, the highest occupied molecular orbital (HOMO) and lowest unoccupied molecular orbital (LUMO) of monomeric **B-2TPA** were delocalized in the same molecule, while those of dimeric **B-2TPA** were delocalized in different molecules. This suggests that both ICT and intermolecular charge transfer exist in dimeric **B-2TPA** [40]. Moreover, the energy gaps between HOMO and LUMO (ΔE) of monomeric and dimeric **B-2TPA** were 3.469 eV and 3.256 eV, respectively. The lower ΔE indicates that **B-2TPA** NPs are more easily excited by laser irradiation [41].

Furthermore, the lowest excited singlet state (S_1) and excited triplet state (T_n) energy levels of monomeric and dimeric **B-2TPA** were analyzed *via* time-dependent density functional theory (TD-DFT) calculations at TD-B3LYP-D3BJ/6-311G*. As shown in Fig. 3d, monomeric **B-2TPA** only had one ISC channel from S_1 to T_1, while dimeric **B-2TPA** had two channels (from S_1 to T_1 or T_2). Their smallest energy gap between S_1 and T_1 (ΔE_{ST}) were 0.937 eV and 0.790 eV, respectively, demonstrating intermolecular aggregation induces lower ΔE_{ST}, which can effectively improve the ISC efficiency of **B-2TPA** NPs, enabling its $^1O_2$ QY higher than **B-2TPA** [42].

The photothermal conversion ability of **B-2TPA** NPs was also studied. As shown in Figs. 3e and f, the increase in temperature of **B-2TPA** NPs aqueous solution depended on its concentration and the laser power. The temperature of 8 μmol/L **B-2TPA** NPs aqueous solution increased from 24.8 °C to 55.1 °C after laser irradiation (1.0 W/cm^2) for 10 min. Next, to evaluate the photostability of **B-2TPA** NPs, its time-dependent absorption spectra change was recorded under laser irradiation. As shown in Fig. S16 (Supporting information), the NIR absorption peak of **B-2TPA** NPs only slightly decreased after laser irradiation for 10 min; conversely, ICG was seriously photodegraded after laser irradiation for 3 min, proving that the photostability of **B-2TPA** NPs is higher than ICG. In addition, after five photothermal conversion cycles, the temperature of **B-2TPA** NPs aqueous solution reached 63.5 °C (Fig. 3g), which is a

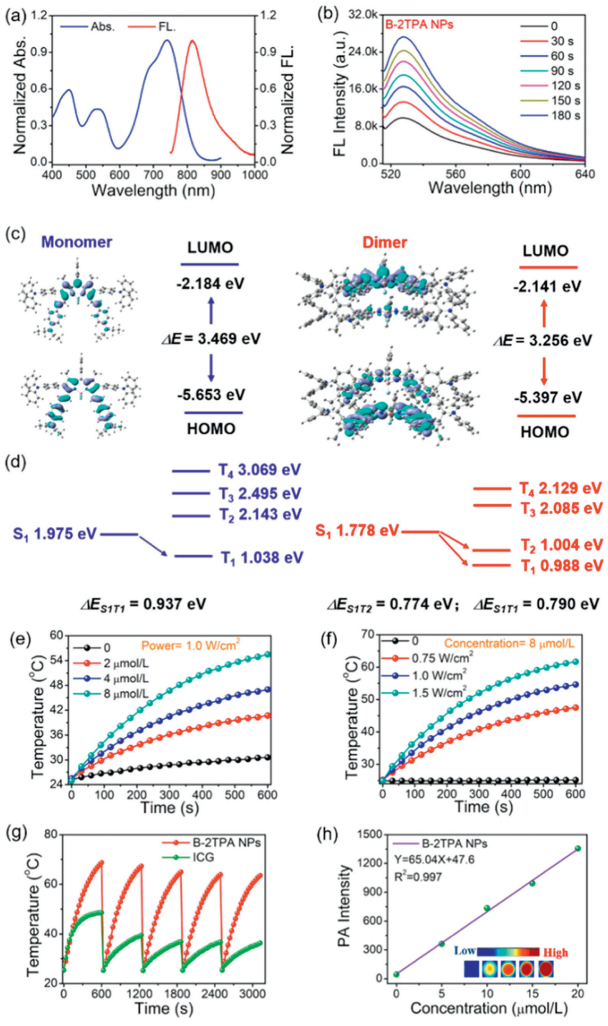

Fig. 3. (a) Normalized vis-NIR absorption and fluorescence spectra of **B-2TPA** NPs in aqueous solution. (b) Fluorescence spectra change of SOSG induced by **B-2TPA** NPs under 735 nm laser irradiation (0.2 W/cm^2) for different times. (c) Diagram showing calculated frontier molecular orbital of monomeric and dimeric **B-2TPA**. $\Delta E = E_{LUMO} - E_{HOMO}$. (d) Calculated energy levels of the singlet and triplet excited states of monomeric and dimeric **B-2TPA**. $\Delta E_{ST} = E_S - E_T$. Irradiation time-dependent temperature variation of **B-2TPA** NPs aqueous solution at different (e) concentrations and (f) laser powers. (g) Photothermal cycle of **B-2TPA** NPs and ICG aqueous solutions during laser irradiation. (h) PA intensities and PA images of **B-2TPA** NPs aqueous solutions at different concentrations.

slight decrease compared to that of ICG and is indicative of the excellent photothermal stability of **B-2TPA**. Based on its heating and cooling curve, the PCE of **B-2TPA** NPs was calculated to be 60.1% ± 0.8% (Fig. S17 in Supporting information) [43], which is also higher than that of **B-2TPA** in dioxane.

Compared with that of **B-2TPA** in dioxane, the fluorescence emission of **B-2TPA** NPs in water was severely quenched (Fig. S18a in Supporting information), indicating that intermolecular aggregation inhibits the radiation decay of **B-2TPA** NPs, while promoting vibrational relaxation to enhance its photothermal conversion ability. Ma *et al.* synthesized B3 by introducing two triphenylamine groups into the α position of BODIPY [44]. When water fraction in THF (f_w) increases from 0 to 50%, the fluorescence peak and intensity of B3 gradually redshifted and weakened, which exhibited TICT effect due to free intramolecular motion. Whereas, when f_w continue to rise from 50% to 90%, its fluorescence intensity obviously increases, exhibiting remarkable AIE performance because strong intermolecular aggregation restricted intramolecular motion, inhibiting the formation of TICT state and decreasing the photothermal conversion ability [45]. However, upon the addition of **B-2TPA** and DSPE-PEG-2000 in water/dioxane mixture solution, as the water content gradually increased, the fluorescence of **B-2TPA** gradually decreased to quenching (Fig. S18b in Supporting information). This indicates the lipophilic microenvironment formed by alkanes of DSPE-PEG-2000 in NPs protects the stable TICT and effective intramolecular motion of **B-2TPA** to further enhance the PCE of **B-2TPA** NPs. Due to its excellent photothermal conversion performance, **B-2TPA** NPs have high PA imaging capability. As shown in Fig. 3h, the PA intensity of **B-2TPA** NPs was positively correlated with NPs concentration.

2,7-Dichlorodihydrofluorescein diacetate (DCFH-DA) was used as an intracellular $^1O_2$ fluorescence probe to confirm the $^1O_2$ production in 4T1 cells after being treated with different treatments. As shown in Fig. 4a and Fig. S19 (Supporting information), only 4T1 cells incubated with **B-2TPA** NPs, followed by irradiation with 735 nm laser, showed significant green fluorescence, which indicated that **B-2TPA** NPs can effectively generate intracellular $^1O_2$ under laser irradiation. Calcein AM/propidium iodide (PI) co-staining was employed to visualize the live and death of 4T1 cells. As shown in Fig. 4b and Fig. S20 (Supporting information), after treatment with PBS, PBS + Laser, and **B-2TPA** NPs, obvious green fluorescence of Calcein AM was observed in 4T1 cells, which suggests that only **B-2TPA** NPs or laser irradiation did not damage the cells, an indication of the low cytotoxicity of **B-2TPA** NPs. On the contrary, after incubating with **B-2TPA** NPs followed by exposure to 735 nm laser, 4T1 cells showed obvious red fluorescence, which confirmed the excellent phototoxicity of **B-2TPA** NPs. Standard methylthiazolyldiphenyl tetrazolium bromide (MTT) experiment was conducted to further confirm the low cytotoxicity and high phototoxicity of **B-2TPA** NPs. The results showed that 16 μmol/L **B-2TPA** NPs + Laser decreased the viability of 4T1 cells to 17% (Fig. 4c), and the corresponding 50% inhibitory concentration (IC_{50}) value was calculated to be 10.4 μmol/L. Flow cytometry results based on annexin V-FITC/7-AAD co-staining further showed that **B-2TPA** NPs + Laser irradiation increased the early apoptotic and later apoptotic/necrotic rates of 4T1 cells to 5.64% and 25.7%, respectively (Fig. 4d). This indicates that the mechanisms of cell death are early apoptosis and later apoptosis/necrosis.

All the animal experiments were approved by the Ethics Committee for Experimental Animal Welfare of Hunan Normal University. **B-2TPA** NPs were injected into 4T1 tumor-bearing mice through the tail vein, and the *in vivo* metabolism and distribution were explored. After intravenous injection of **B-2TPA** NPs, NIR fluorescence images of main organs (heart, liver, spleen, lung, and kidney) and tumor tissues at different times were captured. As shown in Fig. S21 (Supporting information), faint fluorescence was observed in tumor tissue, demonstrating that due to the lack of tumor targeting probe, only a small amount of **B-2TPA** NPs are accumulated in tumor tissues by enhanced permeability and retention (EPR) effect. Thus, the mice were intratumorally injected with **B-2TPA** NPs to investigate *in vivo* optical imaging and anti-tumor ability of **B-2TPA** NPs. This method can effectively enhance the concentration of **B-2TPA** NPs in tumor tissue. The strong NIR fluorescence of the liver and spleen proved that **B-2TPA** NPs accumulated primarily in the liver and spleen, which is attributed to abundant blood perfusion, slow blood flow rate, and active phagocytosis of the reticuloendothelial system [46–48]. Moreover, it gradually increased from 0 to 60 h, indicating that **B-2TPA** NPs in the body are mainly metabolized by the liver and spleen, and require a longer time to clear from the body (Fig. S22 in Supporting information).

As shown in Figs. 4e and f, after being intratumorally injected with **B-2TPA** NPs, the tumor exhibited obvious PA and NIR fluorescence signals, indicating excellent *in vivo* imaging ability of

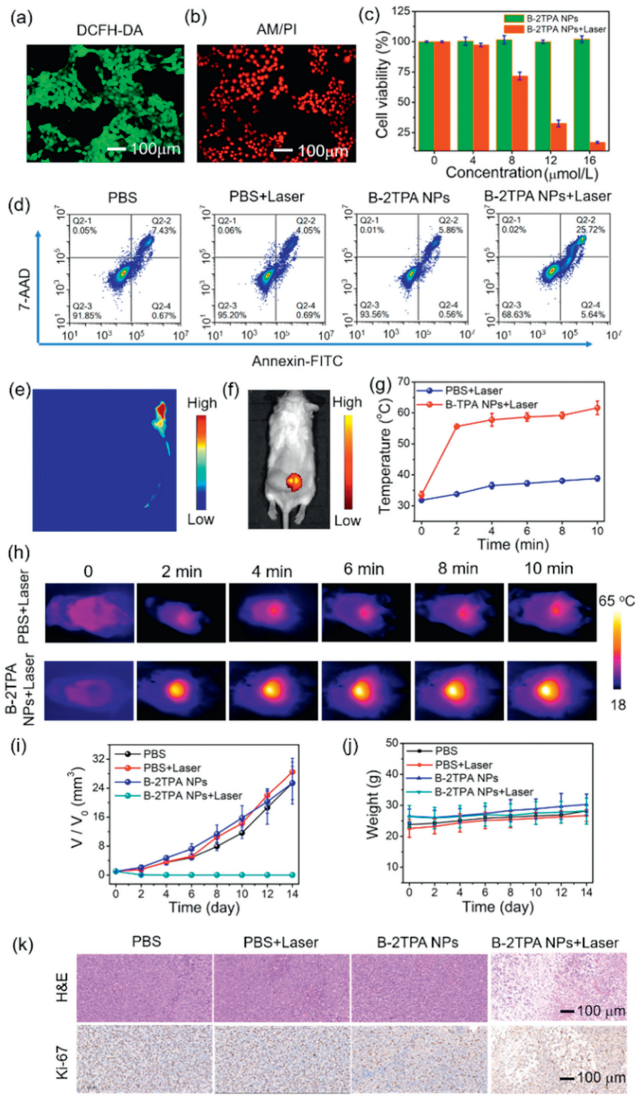

Fig. 4. (a) $^1O_2$ generation in DCFH-DA incubated 4T1 cells treated with **B-2TPA** NPs + Laser. (b) Calcein AM/PI co-stained 4T1 cells treated with **B-2TPA** NPs + Laser. (c) Viability of 4T1 cells incubated with **B-2TPA** NPs at different concentrations with (**B-2TPA** NPs + Laser) or without (**B-2TPA** NPs) laser irradiation. (d) Cell apoptosis observed after **B-2TPA** NPs + Laser treatment. (e) *In vivo* PA and (f) NIR fluorescence images of **B-2TPA** NPs. (g) Infrared thermal images of mice injected with PBS or **B-2TPA** NPs followed by exposure to laser irradiation for 10 min. (h) Temperature variation of tumor tissues after different treatments. (i) Relative tumor volume and (j) body weight of mice after various treatments for 14 days. (k) H&E-staining and Ki-67 expression of tumor tissues under different treatments. Data represent means ± standard deviation (SD) ($n = 5$).

B-2TPA NPs. Moreover, the monitoring by infrared thermography showed that the temperature of tumors injected with **B-2TPA** NPs increased from 33.5 °C to 61.6 °C during the 10 min of illumination, whereas that of tumors injected with PBS only increased from 31.8 °C to 38.0 °C (Figs. 4g and h). The tumors in the experimental group (**B-2TPA** NPs + Laser) were completely removed on the fourth day. Conversely, the relative volume of tumor in the control groups (PBS, PBS + Laser, and **B-2TPA** NPs) has increased by 22-30 times (Fig. 4i). Moreover, the weight of mice gradually increased during monitoring (Fig. 4j), which demonstrates **B-2TPA** NPs have excellent biocompatibility. The histological analysis of tumor tissues in both the experimental and control groups was conducted by H&E and Ki-67 staining experiments. As shown in Fig. 4k, **B-2TPA** NPs + laser destroyed the tumor tissues and inhibited their proliferation. In addition, the H&E staining of main organs confirmed that PBS + Laser and **B-2TPA** NPs groups had no effects on the balance of *in vivo* physiological activities (Fig. S23 in Supporting information).

In conclusion, based on aggregation-induced increase in singlet-triplet ISC and TICT effect, we successfully developed phototheranostic agents (**B-2TPA** NPs) with strong NIR absorption capacity, aggregation-induced enhancement of $^1O_2$ QY, and high PCE. **B-2PTA** was designed and synthesized by introducing *N*,*N*-diethyl aniline and triphenylamine into the skeleton of BODIPY, allowing it to exhibit NIR absorption and fluorescence peaks at 729 and 778 nm, respectively. In addition, **B-2TPA** exhibited a high molar extinction coefficient, excellent photostability, significant TICT effect, and low $^1O_2$ QY (1.8%) and PCE (39.8% ± 0.9%). After being wrapped with DSPE-PEG-2000, the obtained **B-2TPA** NPs showed red-shifted absorption and fluorescence peaks at 751 and 815 nm, respectively. Compared with that of **B-2TPA**, the $^1O_2$ QY of **B-2TPA** NPs enhanced to 6.7% because the intermolecular aggregation-induced decrease of ΔE_{ST} improved ISC efficiency. Moreover, obvious fluorescence quenching and stable TICT effect in the aggregation state facilitate vibrational relaxation, increasing the PCE of **B-2TPA** NPs to 60.1% ± 0.8%. *In vitro* cell experiments demonstrated that through combined PDT and PTT, **B-2TPA** NPs efficiently damaged 4T1 cells. Finally, *in vivo* animal experiments demonstrated that **B-2TPA** NPs could be utilized in NIR fluorescence and PA imaging-guided synergistic PDT and PTT to eliminate tumor tissues.

Declaration of competing interest

The authors declare that they have no known competing financial interests or personal relationships that could have appeared to influence the work reported in this paper.

Acknowledgments

This work was supported by National Key Research and Development Program of China (No. 2022YFA1207600), National Natural Science Foundation of China (Nos. 62175262, 62375289), The Science and Technology Innovation Program of Hunan Province (No. 2022RC1201), The Climb Plan of Hunan Cancer Hospital (No. ZX2021005), The Hunan Provincial Natural Science Foundation of China (No. 2023JJ60464).

Supplementary materials

Supplementary material associated with this article can be found, in the online version, at doi:10.1016/j.cclet.2023.109452.

References

[1] S. Wang, W. Ren, J.T. Hou, et al., Chem. Soc. Rev. 50 (2021) 8887–8902.
[2] X. Qin, F. Li, Y. Zhang, et al., Anal. Chem. 90 (2018) 9381–9385.
[3] X. Yue, B. Wang, M. Lan, et al., Chem. Commun. 59 (2023) 4676–4679.
[4] H. Wang, J. Chang, M. Shi, et al., Angew. Chem. Int. Ed. 58 (2019) 1057–1061.
[5] K. Yang, F. Long, W. Liu, et al., ACS Appl. Mater. Interfaces 14 (2022) 18043–18052.
[6] X. Li, F. Fang, B. Sun, et al., Nanoscale Horiz. 6 (2021) 177–185.
[7] Q. Cheng, Z. Li, Y. Xia, et al., NPG Asia Mater. 11 (2019) 63.
[8] L. Zhang, Y. Geng, L. Li, et al., Chem. Sci. 12 (2021) 5918–5925.
[9] A. Kano, Y. Taniwaki, I. Nakamura, et al., J. Control. Release 167 (2013) 315–321.
[10] W. Park, S.J. Park, K. Na, Biomaterials 32 (2011) 8261–8270.
[11] M. Hou, W. Chen, J. Zhao, et al., Chin. Chem. Lett. 33 (2022) 4101–4106.
[12] J. Jin, Y. Zhu, Z. Zhang, et al., Angew. Chem. Int. Ed. 57 (2018) 16354–16358.
[13] E.A. Owens, M. Henary, G. El Fakhri, et al., Acc. Chem. Res. 49 (2016) 1731–1740.
[14] P. Xue, R. Yang, L. Sun, et al., Nano-Micro Lett. 10 (2018) 74.
[15] L. Cheng, W. He, H. Gong, et al., Adv. Funct. Mater. 23 (2013) 5893–5902.
[16] N. Jing, Z. Zhou, W. Xiong, et al., Chin. Chem. Lett. 32 (2021) 3948–3953.
[17] Y. Wan, G. Lu, W.C. Wei, et al., ACS Nano 14 (2020) 9917–9928.
[18] B. Lu, Y. Huang, Z. Zhang, et al., Mater. Chem. Front. 6 (2022) 2968–2993.
[19] Z. Cheng, T. Zhang, W. Wang, et al., Chin. Chem. Lett. 32 (2021) 1580–1585.

[20] R. Jiang, J. Dai, X. Dong, et al., Adv. Mater. 33 (2021) 2101158.
[21] J. Zhang, S. Mukamel, J. Jiang, J. Phys. Chem. B 124 (2020) 2238–2244.
[22] J. Zhao, K. Yan, G. Xu, et al., Adv. Funct. Mater. 31 (2021) 2008325.
[23] G. Xu, C. Li, C. Chi, et al., Nat. Commun. 13 (2022) 3064.
[24] S. Liu, Y. Li, R.T. Kwok, Chem. Sci. 12 (2021) 3427.
[25] R. Liu, J. Liu, W. Xu, et al., Adv. Mater. 35 (2023) 2303212.
[26] D. Xi, M. Xiao, J. Cao, et al., Adv. Mater. 32 (2020) 1907855.
[27] Z.R. Grabowski, K. Rotkiewicz, W. Rettig, Chem. Rev. 103 (2003) 3899–4032.
[28] X. Lv, C. Gao, T. Han, et al., Chem. Commun. 56 (2020) 715–718.
[29] C. Wang, W. Chi, Q. Qiao, et al., Chem. Soc. Rev. 50 (2021) 12656–12678.
[30] S. Liu, X. Zhou, H. Zhang, et al., J. Am. Chem. Soc. 41 (2019) 5359–5368.
[31] Z. Zhao, C. Chen, W. Wu, et al., Nat. Commun. 10 (2019) 768.
[32] B. Li, E Pang, S. Zhao, et al., Chem. Biomed. Imaging 1 (2023) 541–549.
[33] J. Ma, Z. Liu, Z. Wang, et al., Mater. Chem. Front. 1 (2017) 2547–2553.
[34] Y. Zhang, M. Shi, Z. Yan, et al., Adv. Healthc. Mater. 9 (2020) 2001042.
[35] K. Li, X. Duan, Z. Jiang, et al., Nat. Commun. 12 (2021) 2376.
[36] Z.R. Grabowski, K. Rotkiewicz, A. Siemiarczuk, J. Lumin. 18-19 (1979) 420-424.
[37] X.Y. Shen, W. Yuan, Y. Liu, et al., J. Phys. Chem. C 116 (2012) 10541–10547.
[38] J. Cao, Q. Liu, S. Bai, et al., ACS Appl. Mater. Interfaces 11 (2019) 29814–29820.
[39] D. Wu, H.C. Daly, E. Conroy, et al., Eur. J. Med. Chem. 161 (2019) 343–353.
[40] W. Hu, X. Miao, H. Tao, et al., ACS Nano 13 (2019) 12006–12014.
[41] X. Li, L. Liu, S. Li, et al., ACS Nano 13 (2019) 12901–12911.
[42] H. Ma, Y. Lu, Z. Huang, et al., J. Am. Chem. Soc. 144 (2022) 3477–3486.
[43] X. Xing, K. Yang, B. Li, et al., J. Phys. Chem. Lett. 13 (2022) 7939–7946.
[44] H. Gao, Y. Gao, C. Wang, et al., ACS Appl. Mater. Interfaces 10 (2018) 14956–14965.
[45] S. Liu, C. Chen, Y. Li, et al., Adv. Funct. Mater. 30 (2020) 1908125.
[46] W. Zhang, B. Hao, C. Gao, et al., Eur. J. Pharm. Biopharm. 179 (2020) 206–220.
[47] K.M. Tsoi, S. MacParland, X. Ma, et al., Nat. Mater. 15 (2016) 1212–1221.
[48] Z. Li, Y. Zhu, H. Zeng, et al., Nat. Commun. 14 (2023) 14337.